

Electromagnetic Gyrokinetic Simulations

S.E. Parker, Y. Chen and W. Wan

University of Colorado, Boulder, CO

B.I. Cohen and W.M. Nevins

Lawrence Livermore National Laboratory, Livermore, CA

October 30, 2003

Abstract

A new electromagnetic kinetic electron δf particle simulation model has been demonstrated to work well at large values of plasma β times the ion-to-electron mass ratio [Y. Chen and S.E. Parker, *J. Comput. Phys.* **198** 463 (2003)]. The simulation is three-dimensional using toroidal flux-tube geometry and includes electron-ion collisions. The model shows accurate shear Alfvén wave damping and microtearing physics. Zonal flows with kinetic electrons are found to be turbulent with the spectrum peaking at zero and having a width in the frequency range of the driving turbulence. This is in contrast with adiabatic electron cases where the zonal flows are near stationary, even though the linear behavior of the zonal flow is not significantly affected by kinetic electrons. Zonal fields are found to be very weak, consistent with theoretical predictions for β below the kinetic ballooning limit. Detailed spectral analysis of the turbulence data are presented in the various limits.

1 Introduction

Recently, a new electromagnetic gyrokinetic simulation model has been developed that works well with a realistic mass ratio and at β 's typical of tokamak plasmas[1, 2]. Here, new linear and nonlinear results using this simulation model are reported. This simulation has been linearly benchmarked in toroidal geometry with the continuum codes GS2[3] and GYRO [4] and shows good agreement. Until recently, three-dimensional gyrokinetic particle simulations with realistic geometry have used the adiabatic electron approximation[5, 6, 7, 8]. Continuum models[3, 9, 4] have previously reported

electromagnetic results. Both continuum and δf particle-in-cell (PIC) models may be of value in various limits. Both models, together, provide an important nonlinear cross-check. PIC models are typically more efficient at solving kinetic problems that require fine phase-space resolution[10]. Hence, are useful for ensuring convergence in terms of resolving the five-dimensional phase space.

The difficulty with a fully kinetic treatment of electrons in gyrokinetic particle simulations using the δf -method arises from the fact that for typical tokamak plasmas, where the electron and ion temperatures are of similar magnitude, the electrons move a factor of $\sim \sqrt{m_i/m_e}$ (m_i and m_e are the masses of the ion and the electron) faster than the ions along the magnetic field. This poses a stringent constraint on the time step, $k_{\parallel} v_{Te} \Delta t \leq 1$. To overcome this constraint a new kinetic electron model that uses a generalized split-weight scheme [11], where the adiabatic part is adjustable, along with a parallel canonical momentum formulation has been developed[12]. This was done in three-dimensional toroidal geometry using field-line-following coordinates[13] and includes electron-ion collisions. The simulation reported here uses a timestep only one-third smaller than the time step typically used in adiabatic electron simulations.

In this paper we present our most recent simulation results on microturbulence with both ion-temperature-gradient and trapped-electron drive for typical H-mode plasmas. The spectral features of this type of turbulence is examined. We focus on wavelengths in the $k_{\perp} \rho_i \sim 0.1 - 1$ range and do not address electron-temperature-gradient (ETG) turbulence on ρ_e scale lengths. This makes the drift-kinetic approximation valid for electrons[3].

We begin by giving a very brief overview of the simulation model. Further details can be found in Refs. [1, 2]. Then, we show that the simulation model works well on two basic electromagnetic test problems: Shear Alfvén wave damping, and the collisionless tearing mode instability. Next, we discuss recent linear and nonlinear results where the ion and electron gradient scale lengths are the same, $\eta_e = \eta_i$, η_{α} is a given species, $\alpha = (i, e)$, ratio of temperature gradient to density gradient. Past reported results used a zero electron-temperature-gradient to avoid ETG drive. It turns out that setting $\eta_e = 0$ was unnecessary. Finally, spectral analysis[14] of the turbulence is given showing the features of zonal flows in the adiabatic and electromagnetic limits.

2 Model equations

Three analytical/numerical techniques are used for direct simulation of kinetic electrons in three-dimensional geometry with electromagnetic perturbations. First, a canonical parallel momentum formulation [15] is used to eliminate numerical instabilities associated with finite-differencing of the $\partial A_{\parallel}/\partial t$ term in the parallel electric field, $E_{\parallel} = -\nabla_{\parallel}\phi - \partial A_{\parallel}/\partial t$. Second, a split-weight method [11, 12] is used for the electrons that permits larger timesteps. Third, careful numerical evaluation of the $(\omega_{pe}^2/c^2)A_{\parallel}$ term that appears in Ampere's law in the canonical parallel momentum formulation permits accurate electromagnetic simulations at moderate β , see Ref. [1] for details.

The canonical momentum formulation of the gyrokinetic equations are used where $p_{\parallel\alpha} = v_{\parallel\alpha} + (q_{\alpha}/m_{\alpha})\langle A_{\parallel}\rangle$ is a canonical coordinate. The gyrokinetic equation is

$$\frac{\partial f_{\alpha}}{\partial t} + \mathbf{v}_{G\alpha} \cdot \nabla f_{\alpha} + \dot{p}_{\parallel\alpha} \frac{\partial f_{\alpha}}{\partial p_{\parallel\alpha}} = C(f_{\alpha}), \quad (1)$$

where $\alpha = i, e$,

$$\dot{p}_{\parallel\alpha} = \frac{q_{\alpha}}{m_{\alpha}} \tilde{\mathbf{b}} \cdot \nabla \langle \phi \rangle - \frac{\mu_{\alpha}}{m_{\alpha}} \tilde{\mathbf{b}} \cdot \nabla B + v_{\parallel\alpha} (\mathbf{b} \cdot \nabla \mathbf{b}) \cdot \mathbf{v}_E + \frac{q_{\alpha}}{m_{\alpha}} \mathbf{v}_{G\alpha} \cdot \nabla \langle A_{\parallel} \rangle, \quad (2)$$

$\mathbf{v}_{G\alpha} = v_{\parallel\alpha} \tilde{\mathbf{b}} + \mathbf{v}_{d\alpha} + \mathbf{v}_E$ is the guiding center velocity. $\tilde{\mathbf{b}} = \mathbf{b} + \frac{\langle \delta \mathbf{B}_{\perp} \rangle}{B}$, $\mathbf{v}_{d\alpha} = \frac{v_{\parallel}^2 + v_{\perp}^2/2}{\Omega_{\alpha} B^2} \mathbf{B} \times \nabla B$ is the drift velocity for low β tokamak plasmas with $\beta \ll 1$, $\mathbf{v}_E = \langle \mathbf{E} \rangle \times \mathbf{b}/B$. Here Ω_{α} is the gyrofrequency. The electrons are described by the drift-kinetic equations due to their small gyro radii, hence $\langle \phi \rangle = \phi$, etc., for electrons. $C(f_{\alpha})$ is the collision operator where only electron-ion collisions are considered and a Lorentzian operator is used [16, 17, 1, 2]. Eq. (1) along with gyrokinetic Poisson equation (quasi-neutrality) and Ampere's equation make a complete set. Details on these equations and the methods used to solve them can be found in Ref. [1].

The simulation is toroidal and uses a low- β magnetic equilibrium with concentric flux surfaces. The magnetic field strength is $B(r, \theta) = B_0(1 - (r/R_0) \cos \theta)$. Field-line-following coordinates are used [13] and (x, y, z) are defined by $x = r - r_0$, $y = (r_0/q_0)(q\theta - \zeta)$ and $z = q_0 R_0 \theta$, where (r, θ, ζ) are the usual toroidal coordinates. R_0 is the major radius at the magnetic axis, r_0 is the minor radius at the center of the simulation domain, and $q_0 = q(r_0)$

the safety factor. The simulation domain along the field line is $2\pi q_0 R_0$ in length. Periodic boundary conditions are used in x and y , while the toroidal boundary condition [13] is used in z . By assuming periodicity in radius at fixed y , relaxation of the background equilibrium temperature and density profiles is prevented, even if no particle and heat sources are used. However, spatially localized perturbations of the temperature and density profiles are free to occur (and do).

3 Shear Alfvén wave and tearing mode tests

Here, we examine two classic low-frequency electromagnetic plasma problems to demonstrate the robustness of the simulation model. First, the linear damping of the shear Alfvén wave. Second, the linear and nonlinear evolution of a collisionless kinetic tearing mode.

The damping of the shear Alfvén wave is primarily due to electron Landau damping and is a good test of kinetic electron electromagnetic physics. This test is done in the uniform plasma slab limit where exact numerical solution to kinetic dispersion relation is possible for comparison with theory. This is an important test of the simulation and this particular problem has been used by many others in developing an electromagnetic kinetic electron model[18, 19, 20, 21]. Figure 1 shows the damping rate versus β . The solid line shows the damping rate from the kinetic dispersion relation (theory) compared to that from simulation shown as triangles. Good agreement between theory and simulation is observed. For this case $k_{\parallel}\rho_i = 7.14 \times 10^{-4}$, $k_y\rho_i = 0.2$, $k_x = 0$, $T_i = T_e$, $m_i/m_e = 1837$, $\delta x = \delta y = 0.5\rho_i$, $\delta z = \pi/(16k_{\parallel})$ and there were 32 electrons per grid cell.

A second important electromagnetic test of our simulation model is the collisionless microtearing mode[22, 23, 24]. Here, we use a two-dimensional bounded slab model and neglect the ion response $\delta n_i = 0$. The dimensionality of the simulation is reduced from three to two by setting $k_z = 0$. An electron current layer is initialized having the form $c_1 \exp - \frac{(x - L_x/2)^2}{a^2}$. Here, c_1 is set to $-en_0 v_{te}$ and $a = 0.5\rho_i$. Fig. 2 shows the total nonlinear saturated A_{\parallel} , contours of A_{\parallel} correspond to traces of the magnetic field lines. Fig. 3 shows the nonlinear evolution of δA_{\parallel} for the fundamental k_y , integrated over all x . Nonlinear saturation is observed and the level agrees fairly well with the theoretical level predicted by Drake and Lee[22]. We have developed an linear

eigenmode calculation of the collisionless microtearing mode. To make the theory tractable, the ion response is neglected and we set $\phi = 0$, so that E_{\parallel} is from induction only. This is similar to what was done by Katanuma and Kamimura[23]. Fig. 4 shows excellent agreement between the gyrokinetic simulation and the eigenmode calculation. For all the microtearing mode results $L_x = 2.5\rho_i$, $L_y = 6.28\rho_i$, $\beta = 0.01$, $m_i/m_e = 1837$ and $c/\omega_{pe} = 0.23\rho_i$. The width of the current layer, a , is varied in Fig. 4 keeping $k_y = 1.0\rho_i^{-1}$ fixed. More details on this tearing mode problem will be reported in a future publication[25].

4 Turbulence simulation results with $\eta_e \neq 0$

Here we present how the growth rate and the ion heat diffusivity scales with R/L_T and β , where R is the major radius, L_T is the temperature gradient scale length and β is the plasma beta. We use typical H-mode parameters from the the DIII-D Cyclone Base Case [26, 27]. We set the ion and electron temperature gradient scale lengths equal to each other (or $\eta_e = \eta_i$) where $\eta_{\alpha} = L_{n\alpha}/L_{T\alpha}$. In past results reported, η_e was set to zero[1, 2]. The equilibrium gradient scale lengths are $R_0/L_n = 2.2$, $R_0/L_{Ti} = R_0/L_{Te} = 6.9$, $T_{0i} = T_{0e}$, $r_0/R_0 = 0.18$, $q_0 = 1.4$, $\hat{s} = (r_0/q_0)(dq/dr) = 0.78$. Figure 5 shows the ion heat diffusivity (squares) and linear growth rate (circles) versus R/L_T with $\eta_e = \eta_i$. A super-critical R/L_T is still present with electromagnetic perturbations and kinetic electrons as was found in adiabatic electron simulations[27, 26]. However, with kinetic electrons, the trapped electron drive cause both the linear growth rate and the nonlinear ion heat flux to be much higher. Both the linear and the up-shifted nonlinear critical gradients are found to be lower with kinetic electrons relative to the adiabatic electron case. The R/L_T scan in Fig. 5 is done using $\beta = 4 \times 10^{-4}$ which is small β and not physically important. For this scan the results are essentially electrostatic.

Figure 6 shows the on heat diffusivity (squares) and linear growth rate (circles) versus β . Only weak finite- β stabilization is observed and there is not much reduction in ion heat transport as well. This result is interesting because it is in contrast to the previously published results in Ref. [2] where ion heat transport was greatly reduced with increasing β below the kinetic ballooning limit. This indicates that one might see reduced transport with increasing β only when the ion temperature profile is more peaked relative

to the electron profile so that $\eta_e \ll \eta_i$.

The ion heat diffusivity, χ_i , is calculated in Figs. 5 and 6 from the ion heat flux $\langle \int d\mathbf{v} \hat{\mathbf{r}} \cdot \mathbf{v}_E \frac{1}{2} m_i v^2 \delta f_i \rangle$ divided by $1/L_{Ti}$. For these results the perpendicular box size was $65.3\rho_i \times 64\rho_i$, the grid number was $64 \times 64 \times 32$. The number of particles per species was 4,194,304 and the time step was $\omega_{ci}\Delta t = 3$. The collisionality was set to $\nu_{ei}L_n/v_{Ti} = 0.136$, and the mass ratio was $m_i/m_e = 1837$.

The experimentally measured ion heat diffusivity for the DIII-D shot (shot #81499 at time $t=4000\text{ms}$, on which the base case parameters are based) is $\chi_i = 0.16$ [27] in the units shown in Figs. 5 and 6. This is lower than the adiabatic electron level and much lower than the results presented here with kinetic electrons. Other effects may be playing a role such as effects such as profile variation, equilibrium shear flows, realistic magnetic equilibrium and impurities. All these effects are not modeled here, hence the discrepancy between simulation and experimental data. Even so, the results presented here indicate that kinetic electrons have a dramatic effect on transport and cannot be simply treated as adiabatic.

5 Spectral analysis of turbulence data

Next, we discuss the spectral features and characteristics of the turbulent fluctuations observed in the simulations. We use the GKV data analysis tools developed by Nevins[14]. The various spectral data will be described in terms of field quantities which are functions of (x, y, z, t) where the coordinates (x, y, z) are the field line following coordinates defined in Sec. 2.

Figs. 7 and 8 show the two-dimensional power spectrum of electrostatic potential for both adiabatic electrons and kinetic electrons. The parameters are the same as in Sec. 3, but 16,777,216 particles were used. Similar analysis has been done using 33,554,432 particles and the results do not change. This diagnostic is obtained by choosing x (radial) and z (along the field line) to be in the center of the domain. Fig. 7 is the result with adiabatic electrons and Fig. 8 is electromagnetic with $\beta = 0.4\%$ and kinetic electrons with $\eta_e = 0$. This value of β is chosen so that the overall fluctuation level is the same for both cases due to finite- β stabilization. The results with kinetic electrons in the electrostatic limit are similar, but the overall amplitudes are much higher due to trapped electron drive without any finite- β stabilization. We will refer to the electromagnetic case with kinetic electrons as the “elec-

tromagnetic case,” but it is important to note that the electrostatic kinetic electron case shows similar features. It is the fact that there are kinetic electrons that makes the spectral features different. From these power spectra, one can clearly see the presence of the Geodesic Acoustic Mode (GAM) and the zonal flow[28, 29] at zero k_y . The turbulent spectrum is also observed at negative phase velocity, in the ion diamagnetic drift direction. The electromagnetic case has more energy in the turbulence region of (k_y, ω) and less in the zonal flow region relative to the adiabatic case. Figs. 6 and 7 are contour plots using the same scale. “a.u.” in the figure signifies that the units are arbitrary, but the same units are used in all spectral plots reported here.

Figs. 8 and 9 show the two-dimensional power spectrum of the flux-surface-averaged electrostatic potential in (k_x, ω) . These diagnostics were taken at fixed y and z in the middle of the simulation domain. Fig. 8 is the adiabatic electron case and Fig. 9 is the electromagnetic kinetic electron case. The adiabatic electron case has zonal flows that are very peaked at $\omega = 0$ and extremely coherent GAMs as well. On the other hand, the electromagnetic case has quite turbulent zonal flows peaked at $\omega = 0$. The width of the zonal flow spectrum corresponds with the correlation time of the driving turbulence. Figs. 10 and 11 show the flux-surface-averaged electrostatic potential as a function of (x, t) . Fig. 10 is the adiabatic electron case, where it is observed that the zonal flow is near stationary after initial, fairly long lived, transients. The time axis for Figs. 10 and 11 correspond to a total time of $1200L_T/c_s$. The fast oscillations correspond to GAM oscillations. In contrast, Fig. 11 shows the electromagnetic case with time-dependent, irregular (turbulent) zonal flows. From Fig. 11, one might assume the zonal flows are oscillatory, but from Fig. 9 it is clear that they are turbulent about $\omega = 0$. Fast GAM oscillations are observed for the electromagnetic case as well.

These differences must be associated with nonlinear physics because we have previously shown that the linear zonal flow dynamics changes little between adiabatic and kinetic electron[2]. The adiabatic electron approximation requires that electron motion is tied to a flux surface. This is not the case with kinetic electrons that can ExB drift across flux surfaces. It has also been shown in reduced fluid models that a non-adiabatic electron response can block the low- k condensation of fluctuation energy observed in Hasegawa-Mima turbulence[30, 31]. Finally, we have analyzed the flux-surface-averaged $A_{||}$, or zonal fields[32, 33, 34] in a similar fashion. We find the zonal fields to be relatively weak with an amplitude approximately

5 times smaller than the turbulent A_{\parallel} . This is consistent with theoretical predictions in Ref. [33] that show there is a strong shielding effect on the zonal fields that is on the electron skin depth scale[35].

6 Summary

Results from δf PIC simulations of electromagnetic turbulence were presented. The simulation has been benchmarked linearly and shown to perform well on basic electromagnetic plasma problems. Namely, linear shear Alfvén wave damping and linear and nonlinear collisionless microtearing. δf PIC methods are useful for ensuring proper resolution of complicated phase space dynamics. Turbulence simulations of typical H-mode plasmas show that a nonlinear up-shift in the critical gradient is still observed with electromagnetic kinetic electrons, but the overall critical gradient is much lower due to trapped electron drive. Finite- β stabilization is strong when $\eta_e = 0$, but weak when $\eta_e = \eta_i$. This means that β dependence may be stronger in plasmas where the ion temperature profile is more peaked than the electron temperature profile. Spectral properties of kinetic electron turbulence were reported. Zonal flows are found to be more turbulent with kinetic electrons in contrast to near stationary zonal flows with adiabatic electrons. Linear behavior of the zonal flow is similar in both cases. More theoretical work is needed to explain the turbulent zonal flows with kinetic electrons. Zonal fields are found to be weak, consistent with theoretical predictions.

Acknowledgments

Thanks to V. Decyck, J.N. Leboeuf, UCLA and D. Shumaker, LLNL for helpful collaborations. This work is part of the Summit Framework¹, Computational Center for the Study of Plasma Microturbulence, an Office of Fusion Energy Sciences, United States Department of Energy, Scientific Discovery through Advanced Computing (SciDAC) Project. Thanks to S.T. Jones, Univ. of Colorado, Boulder.

¹<http://www.nersc.gov/scidac/summit>

References

- [1] Y. Chen and S. E. Parker, J. Comput. Phys. **189**, 463 (2003).
- [2] Y. Chen, S. E. Parker, B. Cohen, A. Dimits, W. Nevins, D. Shumaker, V. Decyk, and J. Leboeuf, Nucl. Fusion **43**, 1121 (2003).
- [3] W. Dorland, F. Jenko, M. Kotschenreuther, and B. Rogers, Phys. Rev. Lett. **25**, 5579 (2000).
- [4] J. Candy and R. Waltz, J. Comput. Phys. **186**, 545 (2003).
- [5] S. Parker, W. Lee, and R. Santoro, Phys. Rev. Lett. **71**, 2042 (1993).
- [6] A. Dimits, T. Williams, J. Byers, and B. Cohen, Phys. Rev. Lett. **77**, 71 (1996).
- [7] R. Sydora, V. Decyk, and J. Dawson, Plasma Phys. Controlled Fusion **38**, A281 (1996).
- [8] Z. Lin, T. Hahm, W. Lee, W. Tang, and R. White, Science **281**, 1835 (1998).
- [9] F. Jenko, Comp. Phys. Comm. **125**, 196 (2000).
- [10] S. Vladlamani, S. Parker, Y. Chen, and C. Kim, private communication, submitted to Comp. Phys. Comm. (2003) .
- [11] I. Manuilskiy and W. W. Lee, Phys. Plasmas **7**, 1381 (2000).
- [12] Y. Chen and S. E. Parker, Phys. Plasmas **8**, 2095 (2001).
- [13] M. A. Beer, S. C. Cowley, and G. W. Hammett, Phys. Plasmas **2**, 2687 (1995).
- [14] W. Nevins, private communication, to be submitted to Phys. Plasmas (2003) .
- [15] T. S. Hahm, W. W. Lee, and A. Brizard, Phys. Fluids **31**, 1940 (1988).
- [16] A. H. Boozer and G. Kuo-Petravic, Phys. Fluids **24**, 851 (1981).
- [17] Y. Chen and R. B. White, Phys. Plasmas **10**, 3591 (1997).
- [18] Z. Lin and L. Chen, Phys. Plasmas **8**, 1447 (2001).
- [19] B. I. Cohen, A. M. Dimits, W. Nevins, Y. Chen, and S. E. Parker, Phys. Plasmas **9**, 251 (2002).

- [20] B. I. Cohen, A. M. Dimits, W. Nevins, Y. Chen, and S. E. Parker, Phys. Plasmas **9**, 1915 (2002).
- [21] W. W. Lee, J. L. V. Lewandowski, T. S. Hahm, and Z. Lin, Phys. Plasmas **8**, 4435 (2001).
- [22] J. Drake and Y. Lee, Phys. Rev. Lett. **39**, 453 (1977).
- [23] I. Katanuma and T. Kamimura, Phys. Fluids **23**, 2500 (1980).
- [24] R. Sydora, Phys. Plasmas **8**, 1929 (2001).
- [25] W. Wan, Y. Chen, and S. Parker, private communication, to be submitted to Phys. Plasmas (2004) .
- [26] S. Parker, C. Kim, and Y. Chen, Phys. Plasmas **6**, 1709 (1999).
- [27] A. Dimits et al., Phys. Plasmas **7**, 969 (2000).
- [28] M. N. Rosenbluth and F. L. Hinton, Phys. Rev. Lett. **80**, 724 (1998).
- [29] F. L. Hinton and M. N. Rosenbluth, Plasma Phys. Controlled Fusion **41**, 653 (1999).
- [30] Y. Liang, , P. Diamond, X. Wang, D. Newman, and P. Terry, Phys. Fluids B **5**, 1128 (1993).
- [31] X. Wang, D. Newman, P. Terry, P. Diamond, and Y. Liang, Phys. Fluids B **5**, 1140 (1993).
- [32] A. Gruzinov and P. Diamond, Phys. Plasmas **3**, 1854 (1996).
- [33] L. Chen, Z. Lin, R. White, and F. Zonca, Nucl. Fusion **41**, 747 (2001).
- [34] P. Gudzar, R. Kleva, A. Das, and P. Kaw, Phys. Plasmas **8**, 3907 (2001).
- [35] F. Zonca, private communication (2003) .

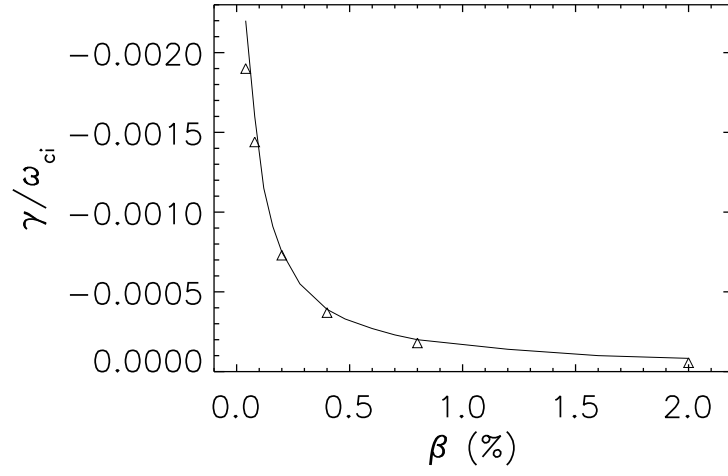


Figure 1: Damping rate versus β for the shear Alfvén wave. The solid line shows the damping rate from the kinetic dispersion relation (theory) compared to that from simulation shown as triangles.

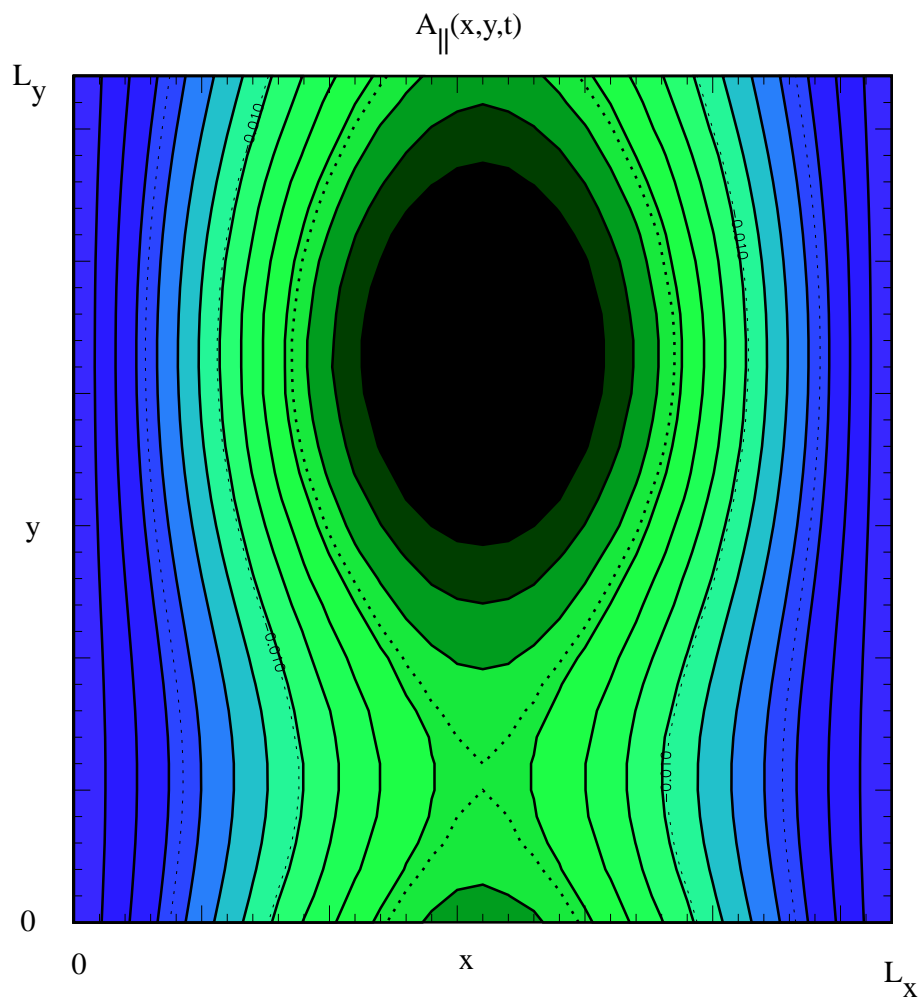


Figure 2: Contour plot of total $A_{\parallel}(x, y)$ showing tearing mode.

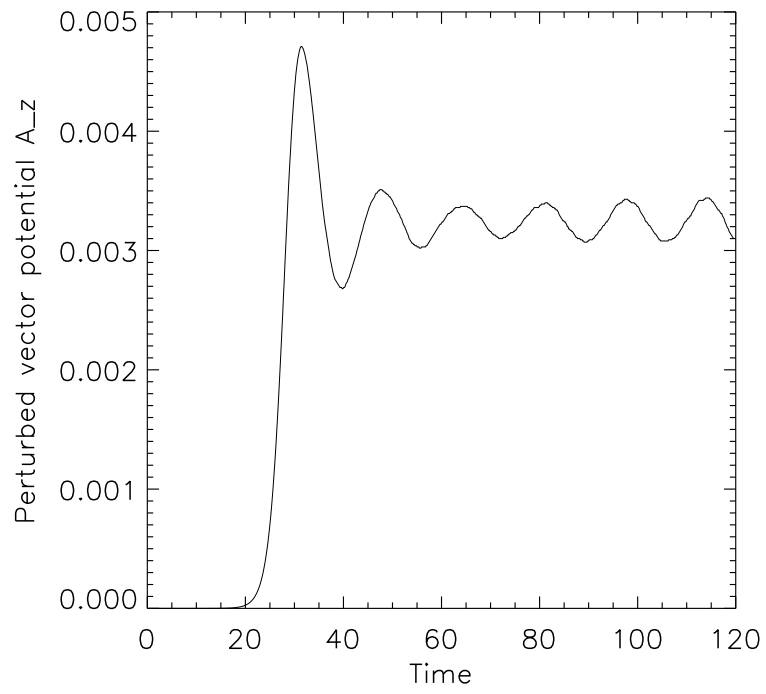


Figure 3: Nonlinear evolution of $\delta A_{\parallel}(k_y = 2\pi/L_y)$.

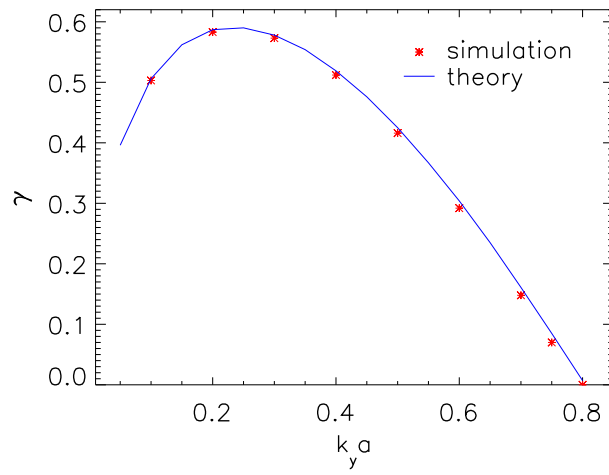


Figure 4: Tearing mode Growth rate versus $k_y a$. Simulation results shown as an asterik and eigenmode calculation shown as the solid line.

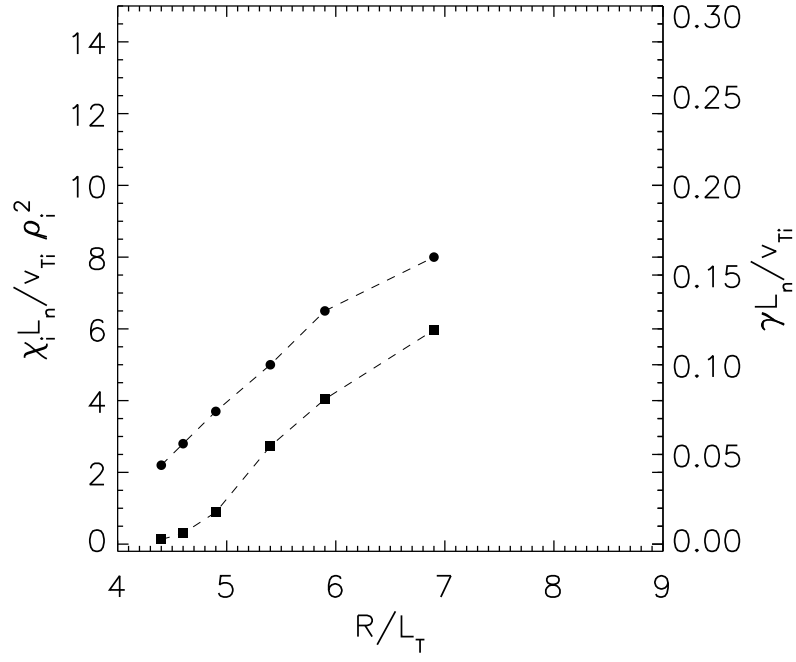


Figure 5: Ion heat diffusivity (squares) and linear growth rate (circles) versus $\frac{R}{L_T}$ scan with $\eta_e = \eta_i$. Sub-critical $\frac{R}{L_T}$ still present with electromagnetic perturbations and kinetic electrons.

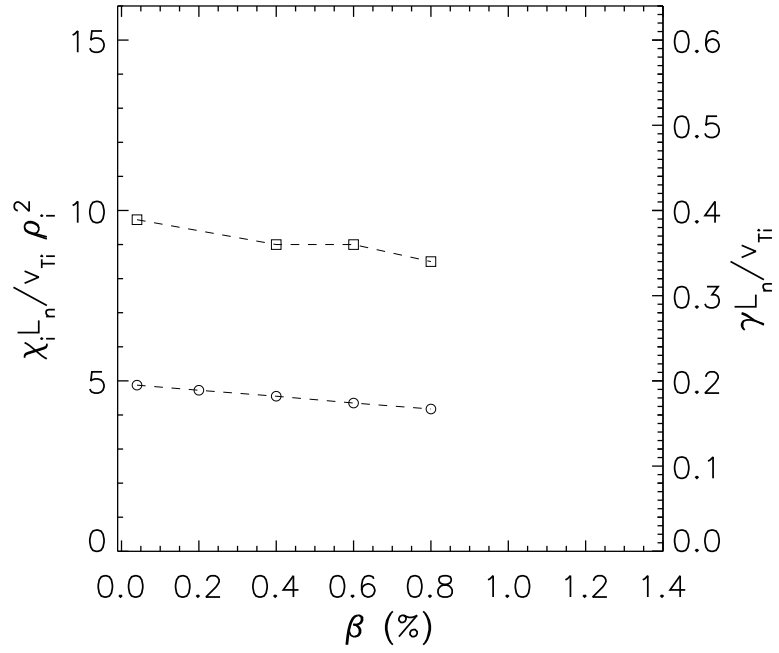


Figure 6: Ion heat diffusivity (squares) and linear growth rate (circles) versus β with $\eta_e = \eta_i$. Weak finite β stabilization and not much reduction in ion heat transport is observed.

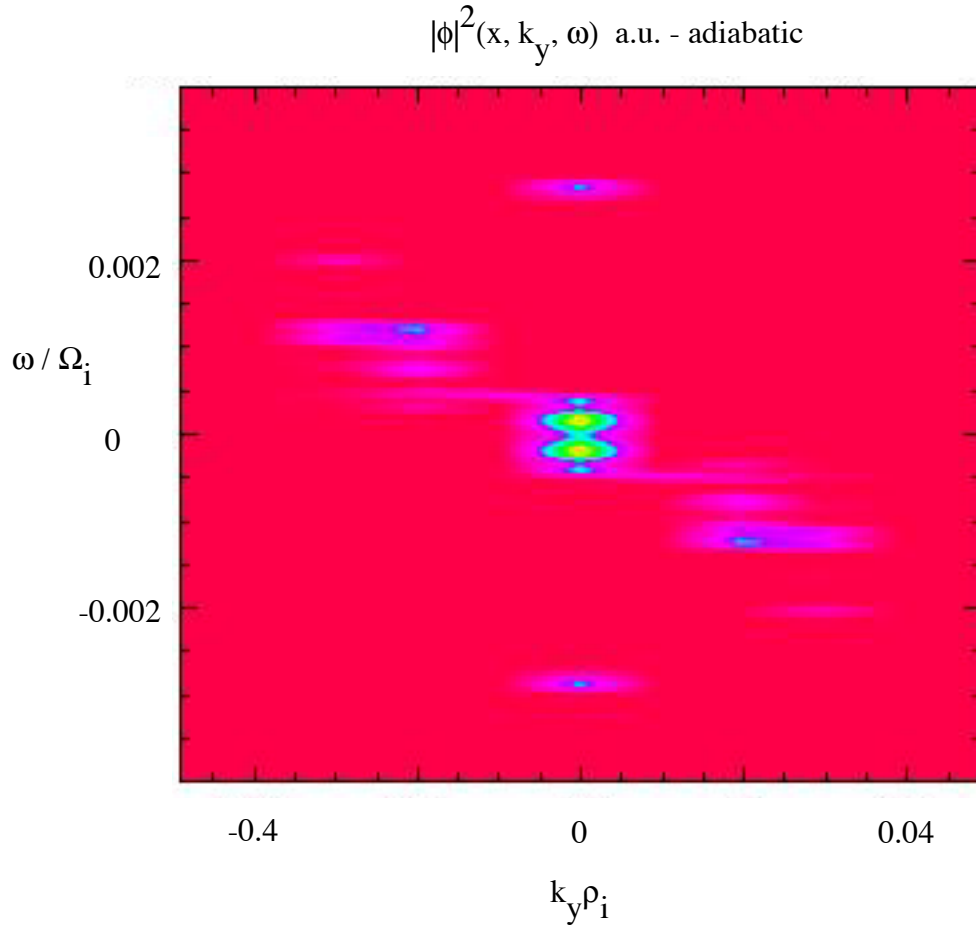


Figure 7: Two-dimensional power spectrum $|\phi|^2(x, k_y, \omega)$ in the adiabatic electron limit showing the dominance of the zonal flows.

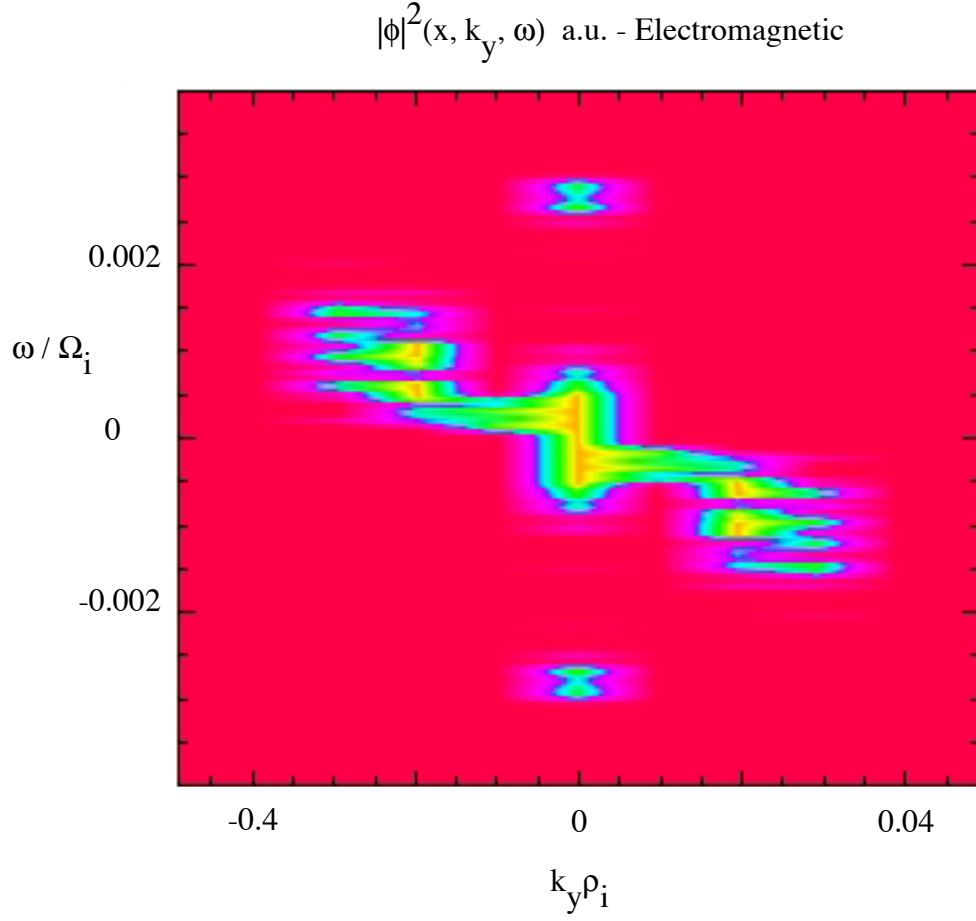


Figure 8: Two-dimensional power spectrum $|\phi|^2(x, k_y, \omega)$ for electromagnetic kinetic electron turbulence showing a more turbulent spectrum overall.

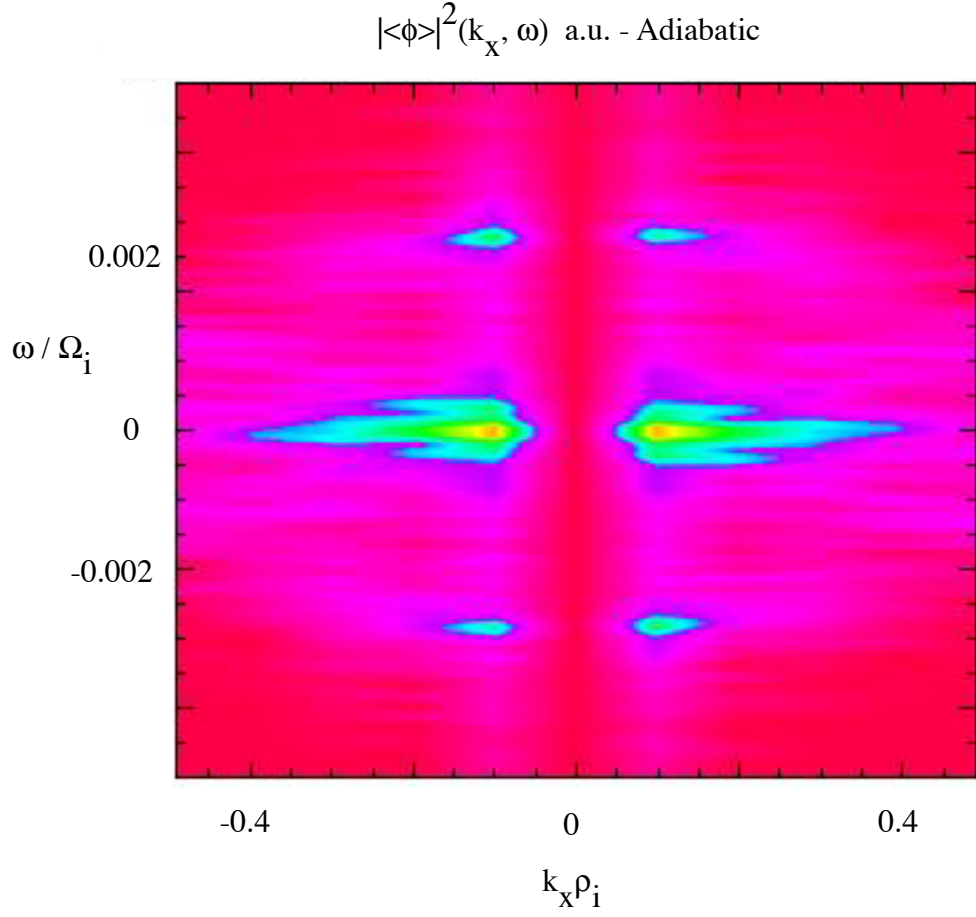


Figure 9: Two-dimensional power spectrum of the flux-surface-averaged electrostatic potential $|\langle \phi \rangle|^2(k_x, \omega)$ for electrostatic adiabatic electron turbulence. Zonal flow spectra is narrowly peaked about $\omega = 0$.

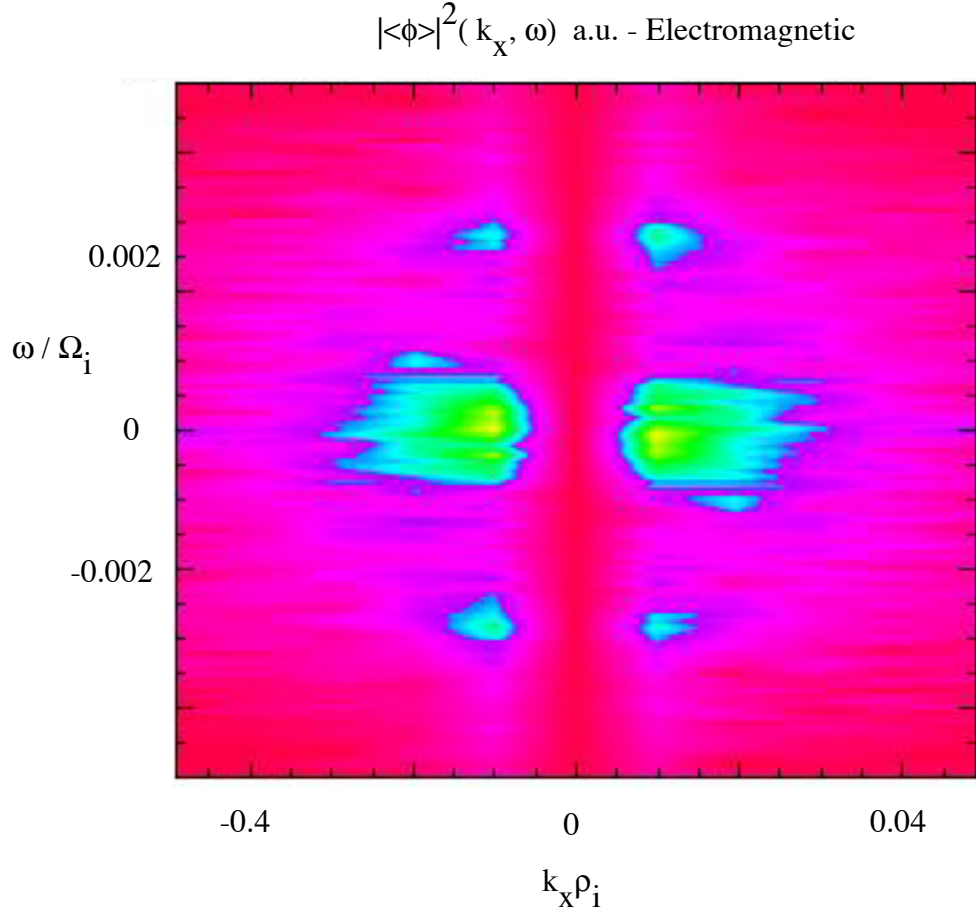


Figure 10: Two-dimensional power spectrum of the flux-surfaced-averaged electrostatic potential $|\langle \phi \rangle|^2(k_x, \omega)$ for electromagnetic kinetic electron turbulence showing a more turbulent zonal flow spectrum.

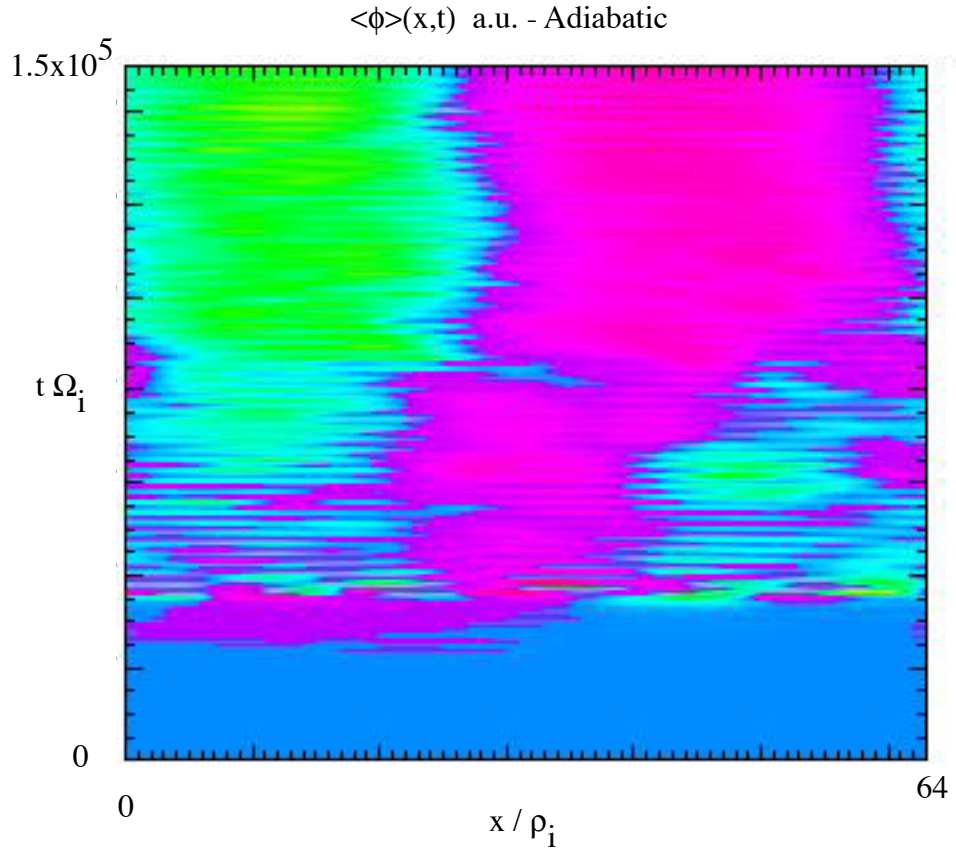


Figure 11: The flux-surface-averaged electrostatic potential for electrostatic adiabatic electron turbulence. Zonal flows are near stationary.

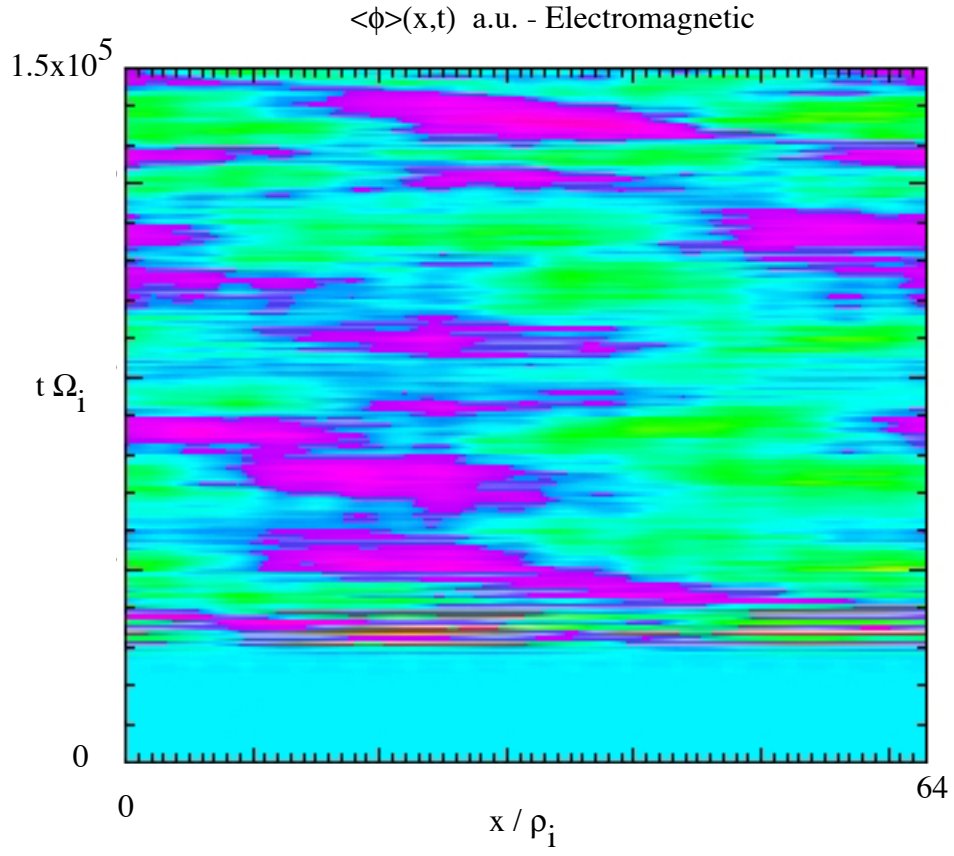


Figure 12: The flux-surface-averaged electrostatic potential for electromagnetic kinetic electron turbulence. Zonal flows are more turbulent.